37. T. C. Ralph, N. K. Langford, T. B. Bell, A. G. White *Phys. Rev. A* **65**, 062324 (2002).
38. H. Hofmann, S. Takeuchi, *Phys. Rev. A* **66**, 024308 (2002).
39. J. L. O'Brien, G. J. Pryde, A. G. White, T. C. Ralph, D. Branning, *Nature* **426**, 264–267 (2003).
40. I. L. Chuang, M. A. Nielsen, *J. Mod. Opt.* **44**, 2455–2467 (1997).
41. J. L. O'Brien *et al*., *Phys. Rev. Lett.* **93**, 080502 (2004).
42. Y. Shi, *Quant. Inf. Comp.* **3**, 84 (2003).
43. M. Tanida, R. Okamoto, S. Takeuchi, *Opt. Exp.* **20**, 15275 (2012).
44. A. Laing, J. L. O'Brien, http://arxiv.org/pdf/1208.2868v1.pdf (2012).
45. C. K. Hong, Z. Y. Ou, L. Mandel, *Phys. Rev. Lett.* **59**, 2044–2046 (1987).
46. L. G. Valiant, *Theor. Comput. Sci.* **8**, 189–201 (1979).
47. N. J. Russell, J. L. O'Brien, A. Laing, http://arxiv.org/pdf/1506.06220.pdf (2015).
48. C. Gogolin, M. Kliesch, L. Aolita, J. Eisert, http://arxiv.org/pdf/1306.3995v2.pdf (2013).
49. S. Aaronson, A. Arkhipov, *Quant. Inf. Comp.* **14**, 1383 (2014).
50. N. Spagnolo *et al*., *Nat. Photonics* **8**, 615–620 (2014).
51. J. Carolan *et al*., *Nat. Photonics* **8**, 621–626 (2014).
52. P. W. Shor, *Proceedings of the 35th Annual Sympo-sium on Foundations of Computer Science* (Society for Industrial and Applied Mathematics, Philadelphia, PA, 1994), pp. 124–134.
53. J. C. F. Matthews *et al*., *Sci. Rep.* **3**, 1539 (2013).
54. M. C. Tichy, K. Mayer, A. Buchleitner, K. Mølmer, *Phys. Rev. Lett.* **113**, 020502 (2014).
55. M. C. Tichy, M. Tiersch, F. de Melo, F. Mintert, A. Buchleitner, *Phys. Rev. Lett.* **104**, 220405 (2010).
56. I. Bengtsson *et al*., *J. Math. Phys.* **48**, 052106 (2007).
57. R. F. Werner, *J. Phys. Math. Gen.* **34**, 7081–7094 (2001).
58. W. Tadej, K. Życzkowski, *Open Syst. Inf. Dyn.* **13**, 133–177 (2006).
59. T. Tao, *Math Res. Lett.* **11**, 251–258 (2003).
60. F. Szollosi, *J. Lond. Math. Soc.* **85**, 616–632 (2012).
61. K. Mattle, M. Michler, H. Weinfurter, A. Zeilinger, M. Zukowski, *Appl. Phys. B* **60**, S111 (2004).
62. A. Peruzzo, A. Laing, A. Politi, T. Rudolph, J. L. O'Brien, *Nat. Commun.* **2**, 224 (2011).
63. A. Laing, T. Lawson, E. Martín López, J. L. O'Brien, *Phys. Rev. Lett.* **108**, 260505 (2012).
64. N. Spagnolo *et al*., *Nat. Commun.* **4**, 1606 (2013).
65. D. J. Thomson *et al*., *IEEE Photon. Technol. Lett.* **24**, 234–236 (2012).
66. J. W. Silverstone *et al*., *Nat. Photonics* **8**, 104–108 (2013).
67. J. P. Sprengers *et al*., *Appl. Phys. Lett.* **99**, 181110 (2011).
68. S. Sohma *et al*., *Optical Communications, 2006. ECOC 2006. European Conference on* (IEEE, New York, 2006), pp. 1–2.

ACKNOWLEDGMENTS

The authors acknowledge support from the Engineering and Physical Sciences Research Council (EPSRC), the European Research Council (ERC), including BBOI, QUCHIP (H2020-FETPROACT-3-2014: Quantum simulation), PIQUE (FP7-PEOPLE-2013-ITN), the Centre for Nanoscience and Quantum Information (NSQI), the U.S. Army Research Office (ARO) grant W911NF-14-1-0133, and the U.S. Air Force Office of Scientific Research (AFOSR). J.C.F.M. was supported by a Leverhulme Trust Early Career Fellowship. J.L.O'B. acknowledges a Royal Society Wolfson Merit Award and a Royal Academy of Engineering Chair in Emerging Technologies.

SUPPLEMENTARY MATERIALS

www.sciencemag.org/content/349/6249/711/suppl/DC1
Materials and Methods
Tables S1 to S5
References (*69*–*72*)

16 April 2015; accepted 26 June 2015
Published online 9 July 2015
10.1126/science.aab3642

Downloaded from http://science.sciencemag.org/ on December 5, 2019

REPORTS

MAGNETISM

Imaging and control of ferromagnetism in $LaMnO_3/SrTiO_3$ heterostructures

X. Renshaw Wang,[1]*†‡ C. J. Li,[2,3]† W. M. Lü,[2] T. R. Paudel,[4] D. P. Leusink,[1] M. Hoek,[1] N. Poccia,[1] A. Vailionis,[5] T. Venkatesan,[2,3,6,7]* J. M. D. Coey,[2,8] E. Y. Tsymbal,[4] Ariando,[2,6] H. Hilgenkamp[1]

Oxide heterostructures often exhibit unusual physical properties that are absent in the constituent bulk materials. Here, we report an atomically sharp transition to a ferromagnetic phase when polar antiferromagnetic $LaMnO_3$ (001) films are grown on $SrTiO_3$ substrates. For a thickness of six unit cells or more, the $LaMnO_3$ film abruptly becomes ferromagnetic over its entire area, which is visualized by scanning superconducting quantum interference device microscopy. The transition is explained in terms of electronic reconstruction originating from the polar nature of the $LaMnO_3$ (001) films. Our results demonstrate that functionalities can be engineered in oxide films that are only a few atomic layers thick.

Modern thin-film deposition techniques enable the synthesis of complex oxide thin films with unit cell (uc)–level control over the thickness. Remarkably sharp phase transitions have been discovered in several systems upon increasing film thickness (*1*–*6*). The most prominent example is the two-dimensional electron gas formed between insulating thin films of $LaAlO_3$ and insulating TiO_2-terminated $SrTiO_3$ (STO) substrates, which occurs at a critical $LaAlO_3$ thickness of 4 uc (*2*). The possibility of selecting a different electronic or magnetic phase by adding a single layer of perovskite unit cells, with a lattice parameter of about 0.4 nm, offers tantalizing opportunities for nanostructured electronic and spintronic devices.

Because various interesting properties have been demonstrated in $LaMnO_3$ (LMO) bulk, thin films, and multilayers, ranging from orbital waves to its use as a catalyst for water splitting (*7*–*11*), LMO is an ideal candidate for observing control of functionalities in oxide heterostructures. It is a Mott insulator with an orthorhombic *Pbnm* structure, based on a $\sqrt{2}a_0$, $\sqrt{2}a_0$, $2a_0$ unit cell where $a_0 \approx 0.39$ nm is the elementary perovskite uc parameter. In stoichiometric LMO, La and Mn are both 3+ ions. The oxide is therefore a polar material that contains alternately charged $(LaO)^{1+}$ and $(MnO_2)^{1-}$ layers. Mn^{3+}, with electronic configuration $t_{2g}^3 e_g^1$ and spin $S = 2$, is a Jahn-Teller ion. If LMO had a perfect cubic perovskite structure, one would expect a conducting ground state, owing to the mobility of the unpaired electron in the degenerate e_g band. However, the e_g orbital degeneracy is lifted by the Jahn-Teller effect, and distorted MnO_6 octahedra line up with alternating long and short Mn-O bonds in the *a*-*b* plane, leading to orbital ordering, which results in electron localization (*12*). As a result of superexchange (*13*), the compound is an A-type antiferromagnet, with Mn spins ferromagnetically aligned within each plane and alternate (001) planes aligned antiferromagnetically. The Néel temperature is ~140 K. The antiferromagnetism is slightly canted in the bulk to produce a weak ferromagnetic moment of ~0.18 μ_B (where μ_B is the Bohr magneton) per uc (*14*–*16*) that is attributed to the antisymmetric Dzyaloshinskii-Moriya (DM) interaction associated with rotation of the MnO_6 octahedra. In thin films, ferromagnetism with a Curie temperature of ~115 K (*17*) accompanied by insulating behavior is often observed. The origin of this ferromagnetism is still unclear, but in addition to the above-mentioned DM mechanism, defects and epitaxial strain can be important factors (*17*–*20*). Here, we report a controllable monolayer-critical magnetic effect, whereby a uniform ferromagnetic state appears in $LaMnO_3$ at a critical thickness of 6 uc.

[1]MESA+ Institute for Nanotechnology, University of Twente, Enschede, Netherlands. [2]NUSNNI-Nanocore, National University of Singapore, Singapore. [3]NUS Graduate School for Integrative Sciences and Engineering, National University of Singapore, Singapore. [4]Department of Physics and Astronomy and Nebraska Center for Materials and Nanoscience, University of Nebraska, Lincoln, NE, USA. [5]Geballe Laboratory for Advanced Materials, Stanford University, Stanford, CA, USA. [6]Department of Physics, National University of Singapore, Singapore. [7]Department of Electrical and Computer Engineering and Department of Materials Science and Engineering, National University of Singapore, Singapore. [8]School of Physics and Centre for Research on Adaptive Nanostructures and Nanodevices, Trinity College, Dublin, Ireland.
***Corresponding author. E-mail: wang.xiao@utwente.nl (X.R.W.); venky@nus.edu.sg (T.V.)** †These authors contributed equally to this work. ‡Present address: Massachusetts Institute of Technology, Cambridge, MA, USA.

In our study, LMO (001) films with thicknesses varying from 1 to 24 uc were grown by means of pulsed laser deposition monitored by reflection high-energy electron diffraction (RHEED), on TiO_2-terminated (001)-oriented STO substrates, in a 10^{-2}-mbar oxygen pressure. LMO films are coherently strained up to 20 uc, as verified by x-ray diffraction and RHEED. All the films were found to be insulating (*21*).

The distribution of local magnetic stray field emanating from the LMO films was imaged by scanning superconducting quantum interference device (SQUID) microscopy (SSM) (*22*) in zero applied field at 4.2 K. The essential part of the SSM is the square pickup loop with an inner size of ~3 × 5 μm^2 (Fig. 1A). During the measurement, the loop was scanned ~2 μm above the sample surface at a contact angle of ~10°. The SSM records the variation of magnetic flux threading the pickup loop, and the flux is converted to magnetic field by dividing by the effective pickup area of ~15 μm^2. The typical flux sensitivity of the SSM is around 14 $\mu\Phi_0$ $Hz^{-1/2}$, where $\Phi_0 = 2 \times 10^{-15}$ Tm^2 is the flux quantum and the bandwidth is 1000 Hz. Because our SSM sensor has a 10° inclination, the measured magnetic stray field component, denoted as B_z, is almost perpendicular to the sample surface. The SSM images are *x*-*y* maps of the magnetic-field values (which are converted to a color scale). The practical sensitivity during measurements set by external noise sources is estimated to be about 30 nT.

Figure 1B shows a typical scan of a 200 by 200 μm^2 area of a 6-uc LMO film grown on STO, with a pixel size of 1 by 1 μm^2. The cooling and measurement were both performed in zero applied field. An irregular pattern of regions with opposite magnetic field orientation was found, presenting a direct image of magnetic field emanating from ferromagnetic domains in the LMO. In Fig. 1, C and D, the local magnitude variations along two orthogonal directions within the plane are presented. Bulk magnetization measurements of ferromagnetic samples found a polarization of the film of 0.3 T (*21*), corresponding to an average moment of 1.6 μ_B per Mn atom. Because the spin-only moment on Mn^{3+} is 4 μ_B, the ferromagnetism appearing in films of LMO cannot be collinear.

Figure 2 shows that a monolayer-sharp transition to ferromagnetism occurs at a critical thickness of 6 uc. Figure 2, A to D, indicates the characteristic domain size evolution with thickness above the critical value. The SSM signals for films with a thickness smaller than the critical value (Fig. 2, E and F) are uniformly much weaker and cannot be resolved; they are two orders of magnitude smaller than the typical root-mean-square (RMS) values of the thicker films. The images for films below the critical thickness are shown on a color scale of one order of magnitude more sensitivity than that used for the ferromagnetic films. The critical thickness for ferromagnetism was confirmed by SSM measurements on another set of samples fabricated in a different growth chamber (*21*). Because a uniform and controllable ferromagnetic state is necessary for device application, the observed critical thickness for ferromagnetism is of particular importance. A critical thickness for ferromagnetism in Sr-doped LMO and $SrRuO_3$ thin films determined with bulk sensitive techniques has been reported (*3*, *4*). However, owing to the lack of domain structure information, characteristics and origin of the transition remain unclear. Using the SSM, Kalisky *et al.* (*6*) performed a comprehensive imaging study of magnetic structures on the interface between $LaAlO_3$ and STO below and above the critical thickness for ferromagnetism at the interface and observed magnetic patches above the critical thickness. Here, we observe an abrupt magnetic transition in which the whole film switches to a ferromagnetic state.

To find out whether the ferromagnetism is indeed solely dependent on the LMO thickness, we fabricated and measured a sample that consisted partly of a 5-uc-thick and partly of a 7-uc-thick LMO film. The sample was prepared by first growing the 5-uc LMO film and then covering half of the surface with a shadow mask while two extra uc of LMO were grown on the exposed surface. As seen from Fig. 3A, the 5-uc area exhibits no SSM signal within the noise level, and the 7-uc area reveals an inhomogeneous magnetic field distribution comparable to that of the regular 7-uc LMO films (Fig. 2C). Figure 3B compares RMS values of the SSM signal for films with different thicknesses; the difference in magnetic field value of films with thicknesses below and above the critical thickness is about two orders of magnitude.

The magnetization orientation of the ferromagnetic LMO films was determined by measuring the magnetization of a 7-uc LMO film grown on STO along different orientations with a vibrating sample magnetometer. During the measurement, the sample is first cooled in a 1-T magnetic field, then the moment is measured during warm-up in 0.1 T. Figure 3C shows the temperature-dependent magnetic moments of a 7-uc LMO film along two different orientations, revealing the in-plane nature of the magnetization. Therefore, the magnetic field pattern imaged by SSM is due to in-plane ferromagnetism. Magnetic moment as a function of temperature for LMO films with different thicknesses is shown in Fig. 3D; 4-uc and 5-uc LMO films show no clear sign of a magnetic moment, indicating an antiferromagnetic or a nonmagnetic state. Because these thinner films show no sign of either ferromagnetism or Curie-law paramagnetism (fig. S10F) in bulk magnetic measurements, yet strong magnetic moments on the Mn sites are still expected to be present, it is likely that the thin LMO films are antiferromagnetic, similar to the bulk (*21*). Furthermore, the

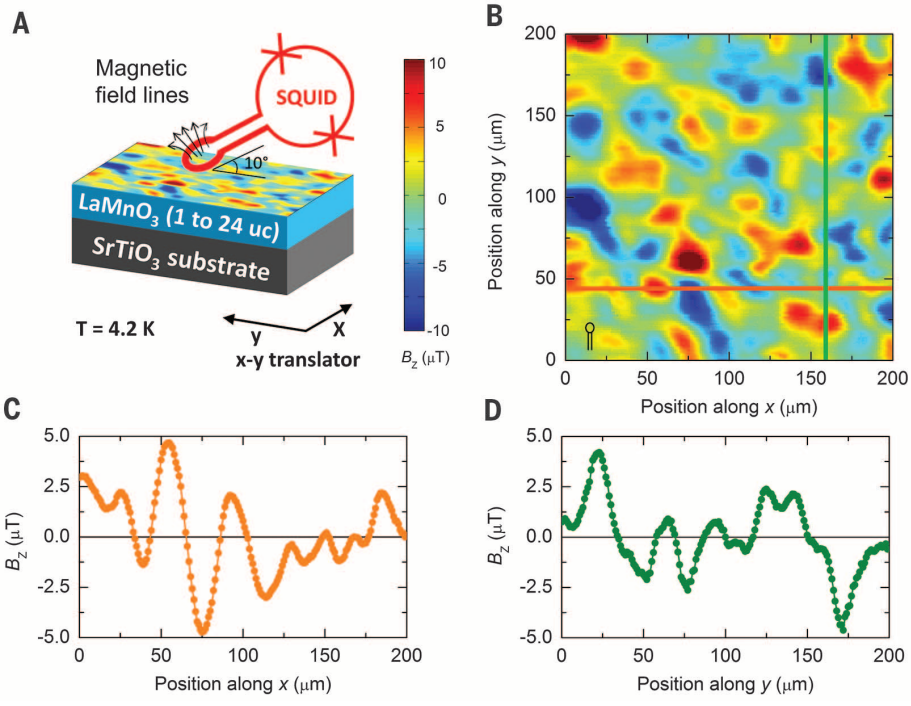

Fig. 1. Scanning SQUID microscopy on a 6-uc LMO film on a STO substrate. (**A**) Schematic of the microscopy technique with sketch of the pickup loop (red). (**B**) Image of the inhomogeneous stray field distribution of a 6-uc LMO film at 4.2 K. The red-yellow peaks in the two-dimensional color map indicate regions where the magnetic stray field exits the sample, and the blue peaks indicate regions where the magnetic stray field enters into the sample. The scan direction is always horizontally from left to right. A sketch (black) in the bottom-left corner of (B) indicates the size of the pickup loop. (**C** and **D**) *x*- (C) and *y*-direction (D) magnetic profiles along the orange and green lines in (B).

Downloaded from http://science.sciencemag.org/ on December 5, 2019

absence of an uncompensated magnetic moment in LMO films with an odd number of unit cells less than 6 (for example, 5) suggests antiferromagnetic order within (001) planes of the sample, rather than the planar antiferromagnetism that is found in the bulk (*21*).

Because of the abruptness of the phase transition and the similarity in polar properties of LMO (001) and $LaAlO_3$ (001) films, it is relevant to consider possible electronic reconstruction, which has been proposed as the mechanism for the abrupt insulator-to-metal transition in the well-studied $SrTiO_3$-$LaAlO_3$ case (*23*). LMO contains alternately charged $(LaO)^{1+}$ and $(MnO_2)^{1-}$ layers, resulting in an internal electric field E_0. A simple first-order estimate for this field is $E_0 = e/2A\varepsilon_0\varepsilon_r$, where e is the elementary charge, A is the unit cell area, ε_0 is the permittivity of vacuum, and ε_r is the dielectric constant of LMO. Taking $\varepsilon_r \sim 70$ at low temperature (*24*), the value of E_0 is 0.85 eV/nm, which will shear both the valence and conduction bands (Fig. 4A). The band gap (E_g) in bulk LMO [about 1.3 eV (*25*)] is smaller than that in bulk STO (3.2 eV), and therefore, charge transfer to eliminate the polar discontinuity occurs entirely within the polar LMO film. This is quite unlike the situation for LAO/STO, where the larger band gap of LAO (5.6 eV) ensures that the electrons are transferred to the STO side of the interface. At a certain thickness $t_c = E_g/E_0 \approx 4$ uc (1.53 nm), the valence band maximum of the LMO reaches the conduction band minimum at the LMO/STO interface, initiating electron transfer from the top to the bottom of the LMO film. Such transfer then decreases the electric field in LMO. The transferred charge as a function of thickness is zero below t_c and increases asymptotically with increasing thickness to 0.5*e* (*21*, *26*). The electron transfer therefore makes the interface region of LMO electron-doped and the top surface region of LMO hole-doped. This is analogous to the electronic phase separation in bulk manganites (*27*), which in our case is stabilized by an intrinsic electric field of the polar LMO film. The doping of LMO tilts the exchange interaction between Mn ions from super-exchange to double exchange and leads to ferromagnetism when a sufficient number of electrons are available. Our density-functional calculations predict that both electron and hole doping of LMO increases the relative energy difference between the antiferromagnetic and ferromagnetic ground states (fig. S8), in agreement with the experimentally reported bulk phase diagram of LMO (*27*–*29*). Thus, electronic reconstruction appears to favor ferromagnetism above a certain critical thickness of LMO. We note that, contrary to the LAO/STO system, where the interface becomes metallic above the critical thickness, our films remain insulating. This is due to the difference in band gap between LAO and LMO. The large band gap of LAO leads to electron transfer to STO, whereas in the LMO/STO case, the electronic reconstruction results in the self-doping of LMO. The self-doping picture is also consistent with a previously reported unaltered Ti^{4+} valence state in $La_{1-x}Sr_xMnO_3$/STO heterojunctions (*29*).

The exact thickness at which the ferromagnetism occurs depends on the spread of the charge. Figure 4B shows an estimated doping charge per Mn atom when all the charge is projected onto just one uc (black curve) and when the charge is spread over 2 uc (red curve). We see that in the latter case, the bulk phase diagram predicts a phase transition from the insulating antiferromagnetic phase to the insulating ferromagnetic phase when the LMO thickness exceeds 6 uc, which is consistent with our experimental observations. The assumption of the charge spread over 2 uc agrees with results of first-principles calculations (*30*) and experimental observations (*29*) that indicate screening of the interface charge in doped LMO.

To verify the feasibility of this electronic reconstruction mechanism, we compared the behavior of 12-uc LMO and $CaMnO_3$ films, because the $Ca^{2+}Mn^{4+}O_3$ (001) film is nonpolar. These films were grown on TiO_2-terminated conducting (001)-oriented 0.1 weight % Nb-doped STO (Nb:STO) substrates and were covered by 2 uc $LaAlO_3$ under the same growth conditions. The 2-uc $LaAlO_3$ capping layer was used to reveal the effect of surface symmetry breaking, and the conducting Nb:STO substrate was used to investigate interface band-bending. By comparing SSM images between $LaAlO_3$-capped LMO grown on Nb:STO (Fig. 4C) and LMO grown on STO (Fig. 2B), we conclude that neither the surface symmetry breaking nor band-bending effects contribute to the critical magnetic behavior. Furthermore, as shown in Fig. 4, C and D, only the LMO films show the magnetic field patterns, whereas the nonpolar $CaMnO_3$ films show no signature of ferromagnetism. Thus, both our theoretical analysis and experimental data suggest

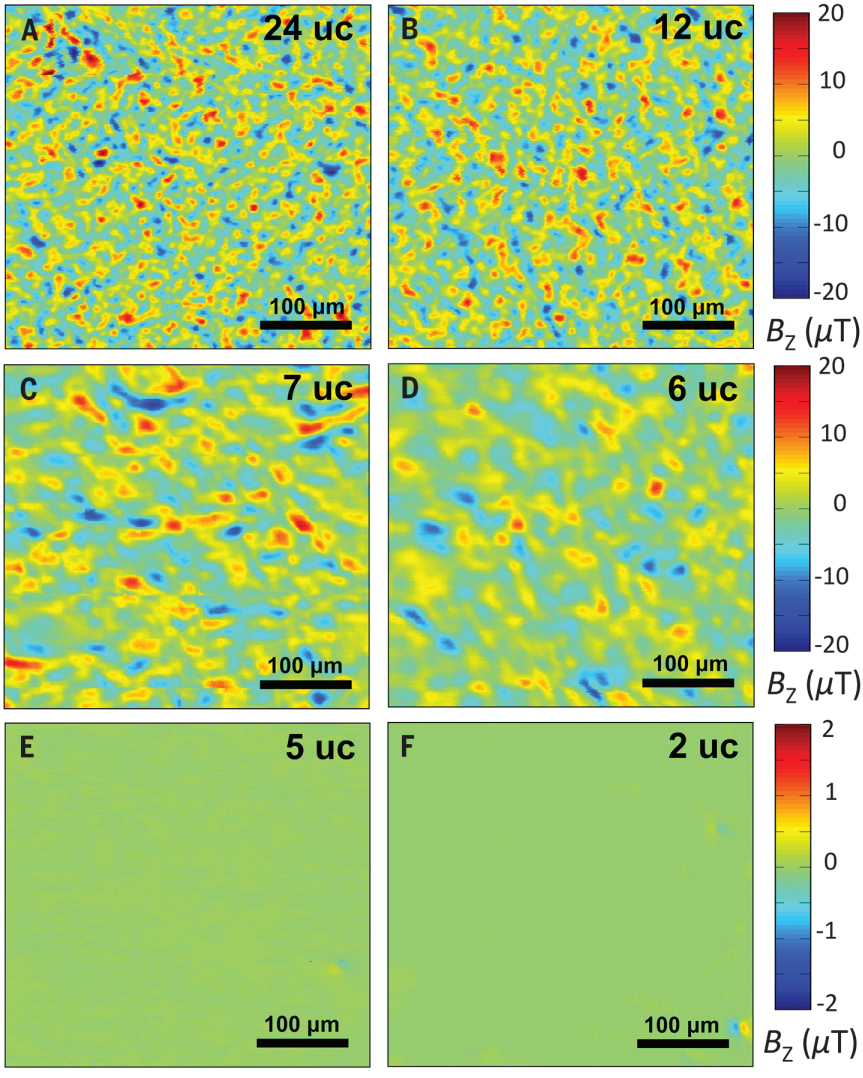

Fig. 2. Critical thickness for ferromagnetism in insulating LMO (001) films grown on STO substrates. All measurements were taken at 4.2 K. (**A** to **D**) Images of magnetic field emanating from LMO films with a thickness of (A) 24 uc, (B) 12 uc, (C) 7 uc, and (D) 6 uc, respectively. (**E** and **F**) Absence of magnetic field for 5-uc (E) and 2 uc (F) LMO. The scale of color bars for 5-uc and 2-uc LMO is one order of magnitude smaller than those of the other images.

Downloaded from http://science.sciencemag.org/ on December 5, 2019

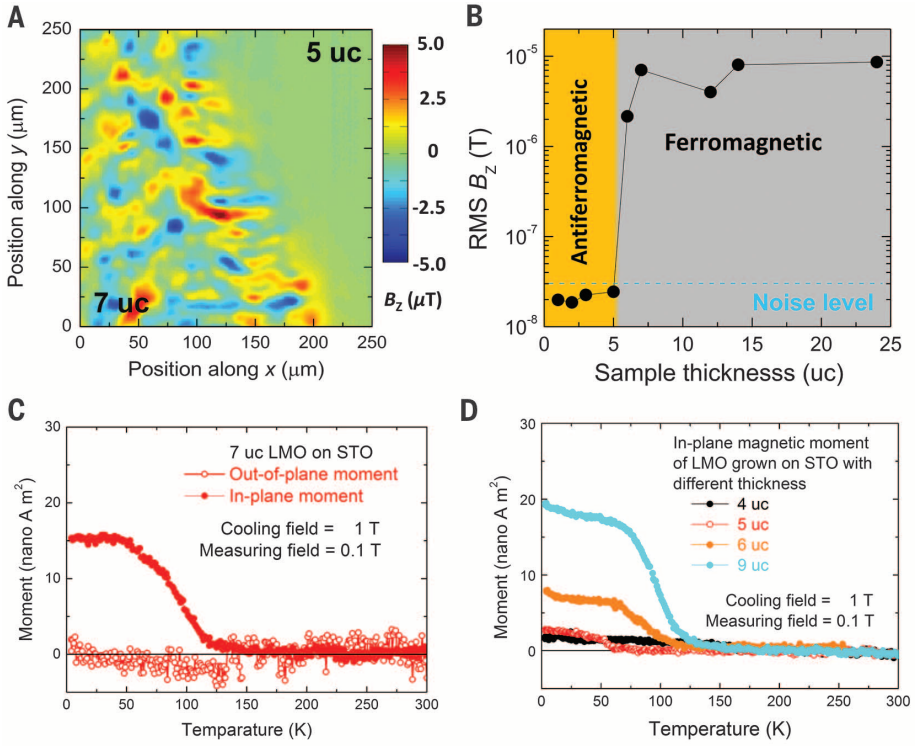

Fig. 3. Abrupt appearance of in-plane ferromagnetism. (**A**) Field distribution measured at 4.2 K in a sample with an upper-right area of 5-uc-thick LMO and a bottom-left area covered by 7-uc LMO. (**B**) RMS values of magnetic field for films with different thicknesses. (**C**) In-plane and out-of-plane magnetic moments of 7-uc LMO grown on STO. The magnetic moment of 7 uc of LMO is found to lie in-plane. (**D**) Magnetic moment of 4-, 5-, 6-, and 9-uc LMO films grown on STO as a function of temperature.

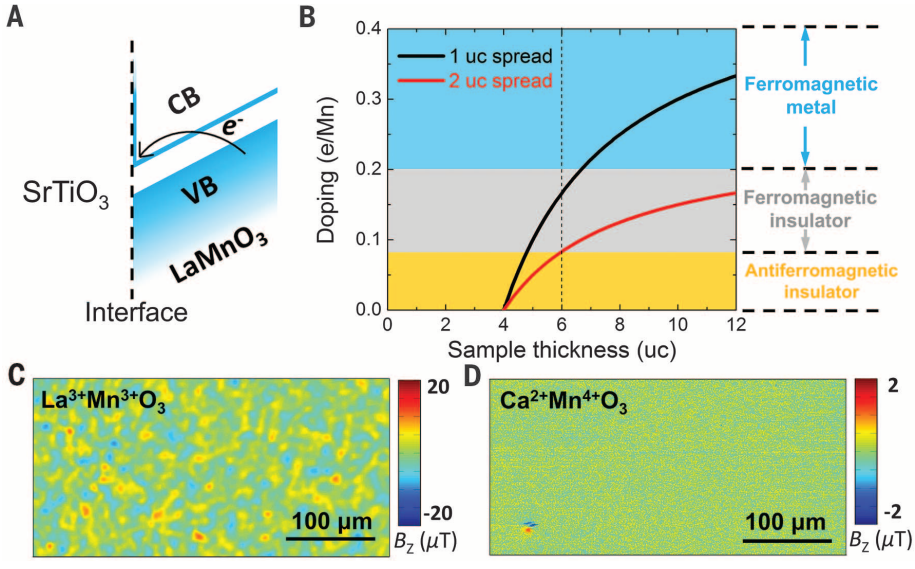

Fig. 4. Analysis of the origin of ferromagnetism in LMO. (**A**) Sketch of the band diagram of electronic reconstruction for LMO (001) film grown on an STO substrate (CB, conduction band; VB, valence band). (**B**) Amount of charge on the Mn site transferred from surface to interfacial layers as a function of LMO thickness. The black curve corresponds to the doping level where all the charge is projected onto just one uc, and the red curve corresponds to the doping level where the charge is spread over 2 uc. The three doping regimes corresponding to the ferromagnetic conducting state (blue area), the ferromagnetic insulating state (gray area), and the antiferromagnetic insulating state (orange area) are adapted from literature for doped bulk LMO (*27*, *28*). (**C**) SSM image of 12-uc $La^{3+}Mn^{3+}O_3$ showing ferromagnetic behavior. (**D**) SSM image of 12-uc $Ca^{2+}Mn^{4+}O_3$ shows no sign of ferromagnetic behavior.

that electronic reconstruction driven by the polar nature of LMO (001) films is a feasible explanation for the abrupt transition to ferromagnetic order in LMO thin films.

REFERENCES AND NOTES

1. J. Junquera, P. Ghosez, *Nature* **422**, 506–509 (2003).
2. S. Thiel, G. Hammerl, A. Schmehl, C. W. Schneider, J. Mannhart, *Science* **313**, 1942–1945 (2006).
3. M. Huijben *et al.*, *Phys. Rev. B* **78**, 094413 (2008).
4. J. Xia, W. Siemons, G. Koster, M. R. Beasley, A. Kapitulnik, *Phys. Rev. B* **79**, 140407 (2009).
5. A. V. Boris *et al.*, *Science* **332**, 937–940 (2011).
6. B. Kalisky *et al.*, *Nat. Commun.* **3**, 922 (2012).
7. E. Saitoh *et al.*, *Nature* **410**, 180–183 (2001).
8. C. H. Kim, G. Qi, K. Dahlberg, W. Li, *Science* **327**, 1624–1627 (2010).
9. J. Suntivich *et al.*, *Nat. Chem.* **3**, 546–550 (2011).
10. M. Gibert, P. Zubko, R. Scherwitzl, J. Iñiguez, J. M. Triscone, *Nat. Mater.* **11**, 195–198 (2012).
11. E. J. Monkman *et al.*, *Nat. Mater.* **11**, 855–859 (2012).
12. H. Sawada, Y. Morikawa, K. Terakura, N. Hamada, *Phys. Rev. B* **56**, 12154–12160 (1997).
13. J. B. Goodenough, *Phys. Rev.* **100**, 564–573 (1955).
14. G. Matsumoto, *J. Phys. Soc. Jpn.* **29**, 606–615 (1970).
15. J. M. D. Coey, M. Viret, S. von Molnar, *Adv. Phys.* **48**, 167–293 (1999).
16. V. Skumryev *et al.*, *Eur. Phys. J. B* **11**, 401–406 (1999).
17. A. Gupta *et al.*, *Appl. Phys. Lett.* **67**, 3494 (1995).
18. A. B. Shah *et al.*, *Adv. Mater.* **22**, 1156–1160 (2010).
19. J. Garcia-Barriocanal *et al.*, *Adv. Mater.* **22**, 627–632 (2010).
20. M. A. Roldan *et al.*, *Microsc. Microanal.* **19**, 1916–1917 (2013).
21. Information on materials and methods is available on *Science* Online.
22. J. R. Kirtley, J. P. Wikswo Jr., *Annu. Rev. Mater. Sci.* **29**, 117–148 (1999).
23. N. Nakagawa, H. Y. Hwang, D. A. Muller, *Nat. Mater.* **5**, 204–209 (2006).
24. P. Mondal, D. Bhattacharya, P. Choudhury, P. Mandal, *Phys. Rev. B* **76**, 172403 (2007).
25. A. Chainani, M. Mathew, D. D. Sarma, *Phys. Rev. B Condens. Matter* **47**, 15397–15403 (1993).
26. W. Son, E. Cho, B. Lee, J. Lee, S. Han, *Phys. Rev. B* **79**, 245411 (2009).
27. E. Dagotto, T. Hotta, A. Moreo, *Phys. Rep.* **344**, 1–153 (2001).
28. H. Fujishiro, T. Fukase, M. Ikebe, *J. Phys. Soc. Jpn.* **67**, 2582–2585 (1998).
29. J. A. Mundy *et al.*, *Nat. Commun.* **5**, 3464 (2014).
30. J. D. Burton, E. Y. Tsymbal, *Phys. Rev. Lett.* **106**, 157203 (2011).

ACKNOWLEDGMENTS

We thank M. S. Golden, A. Brinkman, D. Schlom, M. Huijben, Y. L. Zhao, and W. G. van der Wiel for valuable discussions; D. Veldhuis for assistance in SQUID design and fabrication; and J. R. Kirtley and the IBM T. J. Watson Research Center for providing the microscopy setup. This research was financially supported by the Dutch Foundation for Fundamental Research on Matter (FOM) foundation and through Netherlands Organisation for Scientific Research (NWO)–VICI and Rubicon grants (2011, 680-50-1114). The work at NUS is supported by the Singapore National Research Foundation (NRF) under the Competitive Research Programs (CRP Award no. NRF-CRP 8-2011-06 and CRP Award no. NRF-CRP10-2012-02) and the NUS FRC (AcRF Tier 1 grant no. R-144-000-346-112). Parts of this research were carried out at the Stanford Synchrotron Radiation Lightsource, a Directorate of SLAC National Accelerator Laboratory and an Office of Science User Facility operated for the U.S. Department of Energy Office of Science by Stanford University. The work at University of Nebraska was supported by the NSF through Materials Research Science and Engineering Center (MRSEC, grant no. DMR-1420645). J.M.D.C. acknowledges support from Science Foundation Ireland grant 10/IN1.13006 and the European Union FP7 IFOX Project. All data are available in the supplementary materials.

SUPPLEMENTARY MATERIALS

www.sciencemag.org/content/349/6249/716/suppl/DC1
Materials and Methods
Figs. S1 to S10
References (*31*–*50*)

17 December 2014; accepted 13 July 2015
10.1126/science.aaa5198

Downloaded from http://science.sciencemag.org/ on December 5, 2019

Science

Imaging and control of ferromagnetism in $LaMnO_3/SrTiO_3$ heterostructures

X. Renshaw Wang, C. J. Li, W. M. Lü, T. R. Paudel, D. P. Leusink, M. Hoek, N. Poccia, A. Vailionis, T. Venkatesan, J. M. D. Coey, E. Y. Tsymbal, Ariando and H. Hilgenkamp

Science **349** (6249), 716-719.
DOI: 10.1126/science.aaa5198

Control of magnetism in heterostructures

The interface between two different materials in a heterostructure can exhibit properties unique to either of the two materials alone. A well-known example is a conducting gas that forms when $LaAlO_3$ is grown on $SrTiO_3$, but only if the $LaAlO_3$ layer is at least four unit cells thick. Wang *et al.* report a similarly abrupt magnetic transition in a heterostructure formed by another oxide ($LaMnO_3$) on the same $SrTiO_3$ substrate. Even though bulk $LaMnO_3$ is an antiferromagnet, when six or more unit-cell layers of it were deposited on $SrTiO_3$, it behaved like a ferromagnet.

Science, this issue p. 716

ARTICLE TOOLS http://science.sciencemag.org/content/349/6249/716

SUPPLEMENTARY MATERIALS http://science.sciencemag.org/content/suppl/2015/08/12/349.6249.716.DC1

REFERENCES This article cites 47 articles, 6 of which you can access for free
http://science.sciencemag.org/content/349/6249/716#BIBL

PERMISSIONS http://www.sciencemag.org/help/reprints-and-permissions

Use of this article is subject to the Terms of Service

Science (print ISSN 0036-8075; online ISSN 1095-9203) is published by the American Association for the Advancement of Science, 1200 New York Avenue NW, Washington, DC 20005. The title *Science* is a registered trademark of AAAS.

Copyright © 2015, American Association for the Advancement of Science

Downloaded from http://science.sciencemag.org/ on December 5, 2019